

Cr³⁺-Doped Broadband NIR Garnet Phosphor with Enhanced Luminescence and its Application in NIR Spectroscopy

Liangliang Zhang, Dandan Wang, Zhendong Hao, Xia Zhang, Guo-hui Pan, Huajun Wu, and Jiahua Zhang*

Broadband near-infrared (NIR) phosphor-converted light emitting diode (pc-LED) is demanded for wearable biosensing devices, but it suffers from low efficiency and low radiance. This study reports a broadband NIR Ca_{3-x}Lu_xHf₂Al_{2+x}Si_{1-x}O₁₂:Cr³⁺ garnet phosphor with emission intensity enhanced by 81.5 times. Chemical unit co-substitution of [Lu³⁺–Al³⁺] for [Ca²⁺–Si⁴⁺] is responsible for the luminescence enhancement and further alters the crystal structure and electronic properties of the garnet. Using the optimized phosphor, a NIR pc-LED with photoelectric efficiencies of 21.28% @ 10 mA, 15.75% @ 100 mA and NIR output powers of 46.09 mW @ 100 mA, 54.29 mW @ 130 mA is fabricated. The high power NIR light is observed to penetrate upper arms (≈ 8 cm). For application in NIR spectroscopy, the NIR pc-LED is used as light source to measure transmission spectra of water, alcohol, and bovine hemoglobin solution. These results indicate the NIR garnet phosphor to be a promising candidate for NIR pc-LED.

1. Introduction

In recent years, great efforts have been made to build near-infrared (NIR) spectroscopy technology into wearable devices for biosensing.^[1,2] The technique works by sending a broadband NIR light on food or body that contains certain

compounds such as water, fat, and hemoglobin with characteristic NIR absorption.^[3–6] Therefore, a broadband NIR light source was demanded.^[4] The NIR light emitting diode (LED) was an ideal alternative for fast response and small volume, but it suffered from narrow emission band (<50 nm).^[7] To solve the problem, broadband NIR phosphor-converted LED (pc-LED), inspired by commercial white LED (WLED), was developed. In WLED, a yellow YAG:Ce³⁺ phosphor was coated on a blue LED chip to convert the blue light to white.^[8–10] Similarly, a broadband NIR pc-LED was fabricated by using a broadband NIR phosphor instead of YAG:Ce³⁺. Obviously, an efficient broadband NIR phosphor was required by NIR pc-LEDs.

Some early works on broadband NIR phosphors were conducted by Fuchi et al.^[11–17] Rare-earth ions such as Pr³⁺,


Nd³⁺, Yb³⁺, Sm³⁺, and Tm³⁺ were doped in Bi₂O₃–Sb₂O₃–B₂O₃ glasses. The glass phosphor converted LED showed an NIR emission centered at 1000 nm with 1 mW output power under 815 mA forward current. However, the efficiency of these glass phosphors was low due to f–f forbidden transition of rare-earth ions.^[18–20] Transition metal Cr³⁺ was a promising NIR luminescence center when it located in weak octahedral crystal field. In our previous work, NIR emission properties of Cr³⁺ in garnet structure Ca₂LuZr₂Al₃O₁₂ were studied and an internal quantum efficiency of 69.1% and external quantum efficiency of 31.5% were achieved.^[21] Based on this garnet phosphor, we realized a broadband NIR pc-LED in 750–820 nm spectral range with a photoelectric efficiency of 4.1%, which is larger than 2.9% of traditional tungsten lamp. Afterward, Shao et al. reported Cr³⁺ doped YAl₃(BO₃)₃ phosphor and realized NIR pc-LED with ≈ 26 mW @ 100 mA.^[22,23] Rajendran et al. realized NIR pc-LED with 18.2 mW @ 100 mA by using Cr³⁺-doped La₃Ga₅GeO₁₄ phosphor.^[24] Huang et al. reported Cr³⁺-doped nano-ZnGa₂O₄ broadband NIR phosphor for Mini LEDs.^[25] So far, Cr³⁺-doped broadband NIR phosphors have attracted increasing interests.

The NIR phosphors were still low efficient for applications.^[26,27] Luminescence of Cr³⁺ is originated from transition between outer 3d levels, which is sensitive to both crystal field and electron–phonon coupling.^[28,29] To modify the local crystal

Dr. L. Zhang, Prof. Z. Hao, X. Zhang, Dr. G. Pan, H. Wu, Prof. J. Zhang
State Key Laboratory of Luminescence and Applications
Changchun Institute of Optics
Fine Mechanics and Physics
Chinese Academy of Sciences
3888 Eastern South Lake Road, Changchun 130033, China
E-mail: zhangjh@ciomp.ac.cn

Dr. L. Zhang, Prof. J. Zhang
Center of Materials Science and Optoelectronics Engineering
University of Chinese Academy of Sciences
Beijing 100049, China

Dr. D. Wang
Key Laboratory of Functional Materials Physics and Chemistry
of the Ministry of Education
Jilin Normal University
Siping 136000, China

 The ORCID identification number(s) for the author(s) of this article can be found under <https://doi.org/10.1002/adom.201900185>.

DOI: 10.1002/adom.201900185

field of Cr^{3+} , ion substitution was widely adopted.^[30,31] In recent years, a strategy named “chemical unit co-substitution” was developed from complex polyatomic substitution,^[32] which changes two structural units at the same time. Xia et al. reported new $\text{Ca}_2\text{Mg}(\text{Si}_2\text{O}_7)$ structure by $[\text{Mg}^{2+}\text{-Si}^{4+}]$ unit substituting for $[\text{Al}^{3+}\text{-Al}^{3+}]$ in $\text{Ca}_2\text{Al}(\text{AlSiO}_7)$.^[33] This complex substitution not only modified the crystal field but also changed the electron–phonon coupling effect. Chemical unit co-substitution showed broader adjusting range to find new phosphors.

In this paper, we reported greatly enhanced luminescence of Cr^{3+} in $\text{Ca}_{3-x}\text{Lu}_x\text{Hf}_2\text{Al}_{2+x}\text{Si}_{1-x}\text{O}_{12} \cdot 0.08\text{Cr}^{3+}$ due to chemical unit co-substitution of $[\text{Lu}^{3+}\text{-Al}^{3+}]$ for $[\text{Ca}^{2+}\text{-Si}^{4+}]$ with increasing x value. Valance state and site preference of chromium were found to be changed by chemical unit co-substitution. Crystal structure, electronic, and luminescent properties were discussed. Using the optimized NIR phosphor, an NIR pc-LED with the highest output power and photoelectric efficiency compared to the previous reports was realized. Deep penetration in tissues and NIR spectroscopy applications of the NIR pc-LED were also demonstrated.

2. Results and Discussion

2.1. Structure

The crystalline phase of $\text{Ca}_{3-x}\text{Lu}_x\text{Hf}_2\text{Al}_{2+x}\text{Si}_{1-x}\text{O}_{12}$ belongs to garnet structure with three sites: dodecahedral $\text{Ca}^{2+}/\text{Lu}^{3+}$ site, octahedral Hf^{4+} site, and tetrahedral $\text{Al}^{3+}/\text{Si}^{4+}$ site, as shown in Figure 1. The x value is the nominal percentage of co-substitution of $[\text{Lu}^{3+}\text{-Al}^{3+}]$ for $[\text{Ca}^{2+}\text{-Si}^{4+}]$. Rietveld refinement with the nominal atom occupancy shows good convergence, as listed in Tables S1 and S2 (Supporting Information). With increasing x value, the chemical unit co-substitution of $[\text{Lu}^{3+}\text{-Al}^{3+}]$ substituting for $[\text{Ca}^{2+}\text{-Si}^{4+}]$ is expected. Valance states of the tetrahedral site ($\text{Si}^{4+} \rightarrow \text{Al}^{3+}$) and dodecahedral site ($\text{Ca}^{2+} \rightarrow \text{Lu}^{3+}$) are changed while the total valance is the same. Moreover, the tetrahedral site is transformed from substitution disordered $\text{Si}^{4+} + \text{Al}^{3+}$ at $x = 0$ to ordered Al^{3+} alone at $x = 1$. In contrary, Lu^{3+} substitution for Ca^{2+} in the dodecahedral site results in transformation from substitution ordered Ca^{2+} at $x = 0$ to substitution disordered $\text{Ca}^{2+} + \text{Lu}^{3+}$ at $x = 1$. As shown in Figure 1c, the

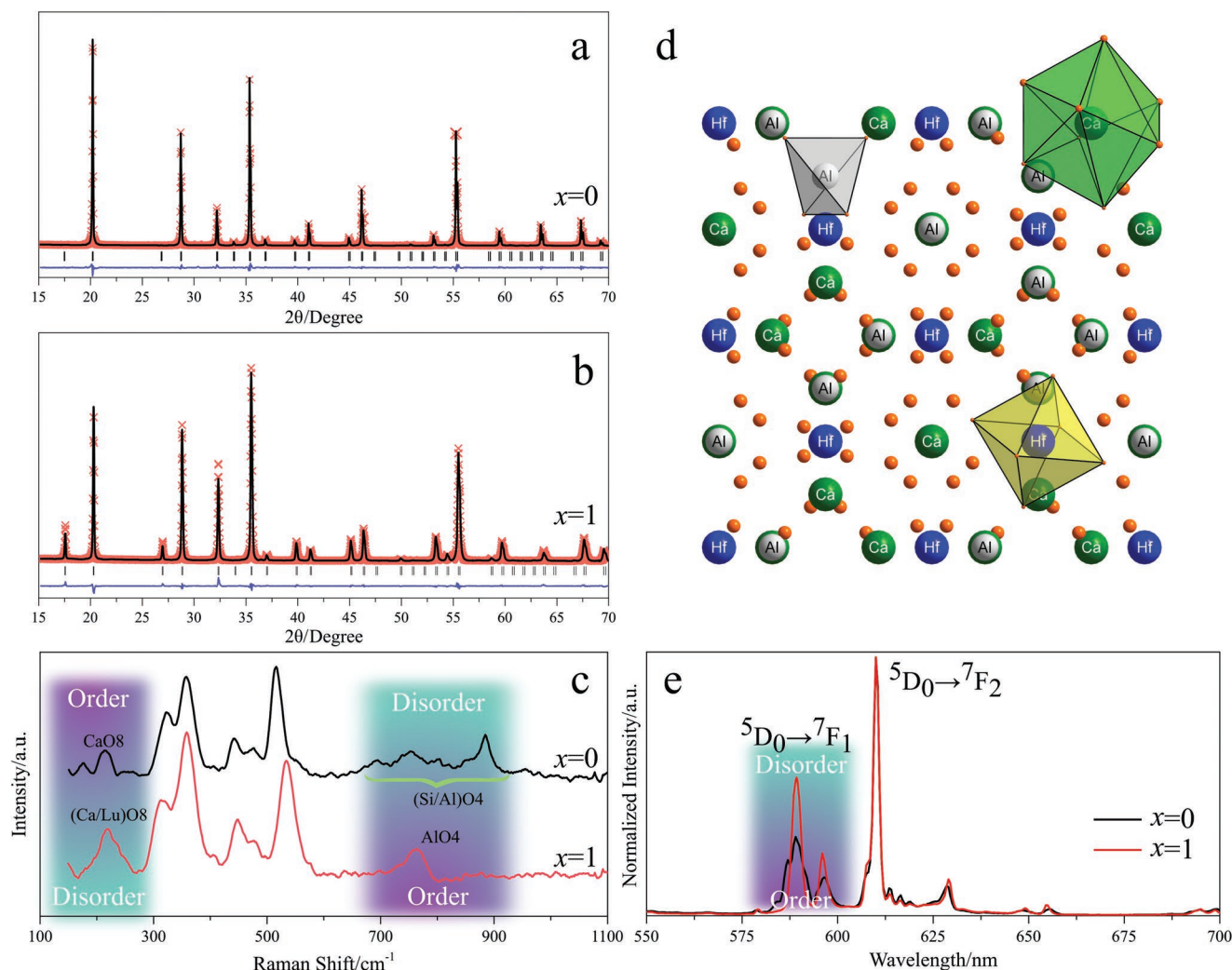


Figure 1. a,b) X-ray diffraction pattern, c) Raman spectra, and d) crystal structure of $\text{Ca}_{3-x}\text{Lu}_x\text{Hf}_2\text{Al}_{2+x}\text{Si}_{1-x}\text{O}_{12}$. e) Emission spectra of $\text{Ca}_{3-x}\text{Lu}_x\text{Hf}_2\text{Al}_{2+x}\text{Si}_{1-x}\text{O}_{12} \cdot 0.01\text{Eu}^{3+}$ excited by 254 nm.

ordered $[\text{CaO}_8]$ is characteristic of two Raman peaks at 176 and 216 cm^{-1} . Inhomogeneous broadening of these Raman peaks is observed when Lu^{3+} is introduced. The disordered $[\text{Al}/\text{SiO}_4]$ tetrahedral site is characteristic of a series of Raman peaks from 690 to 900 cm^{-1} . These peaks degenerate to one Raman peak at 764 cm^{-1} with ordered $[\text{AlO}_4]$ tetrahedral site. As a result, the maximum phonon energy decreases from 886 to 764 cm^{-1} . To observe changes in site symmetry caused by the co-substitution, Eu^{3+} is introduced as a fluorescence probe to occupy the dodecahedral site. As shown in Figure 1e, the emission intensity ratio of ${}^5\text{D}_0 \rightarrow {}^7\text{F}_2$ to ${}^5\text{D}_0 \rightarrow {}^7\text{F}_1$ for $x = 1$ is smaller than that for $x = 0$. The smaller ratio indicates a higher symmetry on the dodecahedral site for $x = 1$ compared with that for $x = 0$.

The electronic structure of $\text{Ca}_{3-x}\text{Lu}_x\text{Hf}_2\text{Al}_{2+x}\text{Si}_{1-x}\text{O}_{12}$ when $x = 0$ and $x = 1$ is calculated by first-principles calculations, as shown in Figure 2. The calculation results show indirect band gaps for both $x = 0$ and $x = 1$, which is proved by the experimental diffuse reflection (DR) spectra in Figure S5b,e (Supporting Information). The band gap is calculated to be 3.95 and 4.0 eV for $x = 0$ and $x = 1$, respectively, and is consistent with the experimental data in Figure S5c,f (Supporting Information). The band gap is almost unchanged with the chemical unit co-substitution. However, the partial density of states (DOS) are different, as shown in Figure 2c,d. The valence band maximums mainly consist of states of O atoms for both $x = 0$ and $x = 1$. However, the conduction band minimum (CBM) of $x = 0$ is hybrid electronic states of Hf^{4+} and Ca^{2+} , while CBM of $x = 1$ is primarily the electronic states of Lu^{3+} . As shown in

Figure 2a,b, CBM charge density distribution of $\text{Ca}_{3-x}\text{Lu}_x\text{Hf}_2\text{Al}_{2+x}\text{Si}_{1-x}\text{O}_{12}$ when $x = 0$ and $x = 1$ are gathered and locate in $\text{Hf}^{4+}\text{--Ca}^{2+}\text{--Hf}^{4+}$ atom channels, while that for $x = 1$ locate in $\text{Lu}^{3+}\text{--Lu}^{3+}$ atom channels.

Bader charge analysis is performed to determine the degree of covalency. As listed in Table S4 (Supporting Information), atomic charges of all the atoms are much smaller than the valence. This indicates a high level of covalency of $\text{Ca}_{3-x}\text{Lu}_x\text{Hf}_2\text{Al}_{2+x}\text{Si}_{1-x}\text{O}_{12}$. The splitting of Ce^{3+} 5d level in $\text{Ca}_{3-x}\text{Lu}_x\text{Hf}_2\text{Al}_{2+x}\text{Si}_{1-x}\text{O}_{12}$ is calculated for evaluating the degree of covalency in this host. The centroid shift (ϵ_c) and crystal field splitting (ϵ_{cfs}), which relate to the covalency and ionicity, respectively, are determined and listed in Table S5 (Supporting Information). One can find that ϵ_c and ϵ_{cfs} of Ce^{3+} -doped $\text{Ca}_{3-x}\text{Lu}_x\text{Hf}_2\text{Al}_{2+x}\text{Si}_{1-x}\text{O}_{12}$ are similar to that of CaSiN_2 , which shows high covalency due to a nitride compound.

2.2. Luminescence

The emission spectra of Cr^{3+} in $\text{Ca}_{3-x}\text{Lu}_x\text{Hf}_2\text{Al}_{2+x}\text{Si}_{1-x}\text{O}_{12}$ ($x = 0, 0.3, 0.6, 1.0$) excited by 460 nm show a broadband that covers 700–1000 nm spectral range, as shown in Figure 3a. It is observed that the intensity increases 81.5 times with blue shift of the emission peak from 855 to 785 nm. To understand the origin of the luminescence enhancement, excitation spectra for separately monitoring 750 and 855 nm (Figure S6a–d, Supporting Information) and emission spectra excited separately by 280 and 460 nm (Figure S6e–h, Supporting Information)

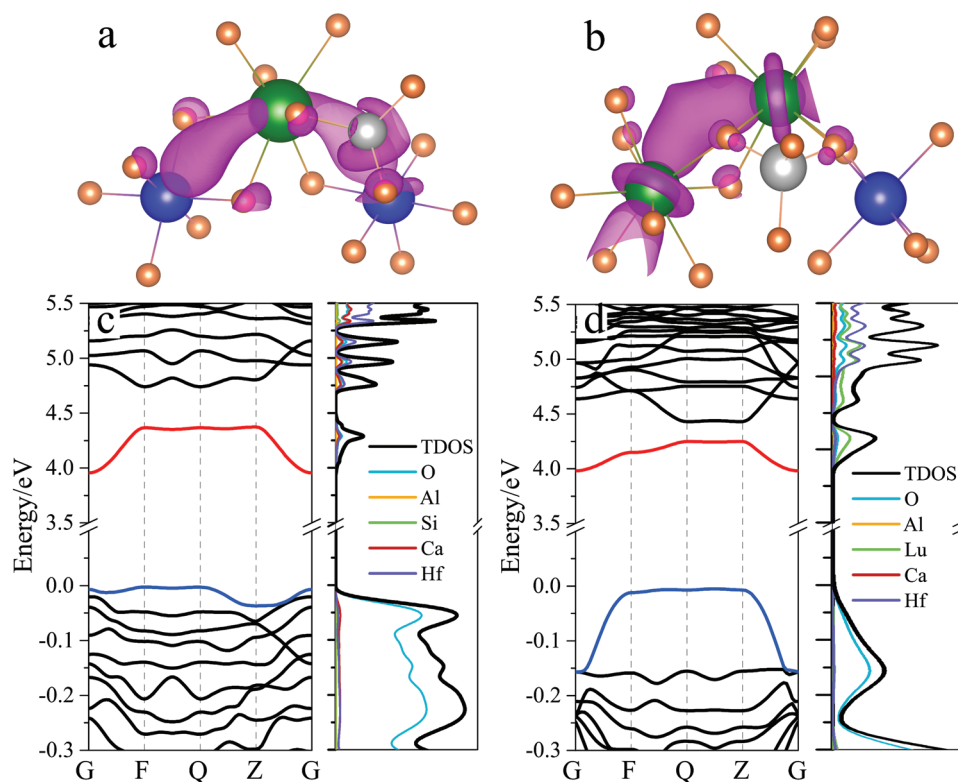


Figure 2. a,b) CBM charge density distribution of $\text{Ca}_{3-x}\text{Lu}_x\text{Hf}_2\text{Al}_{2+x}\text{Si}_{1-x}\text{O}_{12}$ when $x = 0$ and $x = 1$, respectively. The green balls are the dodecahedral site (Ca^{2+} when $x = 0$ and Lu^{3+} when $x = 1$), the blue balls are octahedral site (Hf^{4+} for both $x = 0$ and $x = 1$), and the gray balls are the tetrahedral site (Si^{4+} when $x = 0$ and Al^{3+} when $x = 1$). c,d) Band structures and DOS of $\text{Ca}_{3-x}\text{Lu}_x\text{Hf}_2\text{Al}_{2+x}\text{Si}_{1-x}\text{O}_{12}$ when $x = 0$ and $x = 1$, respectively.

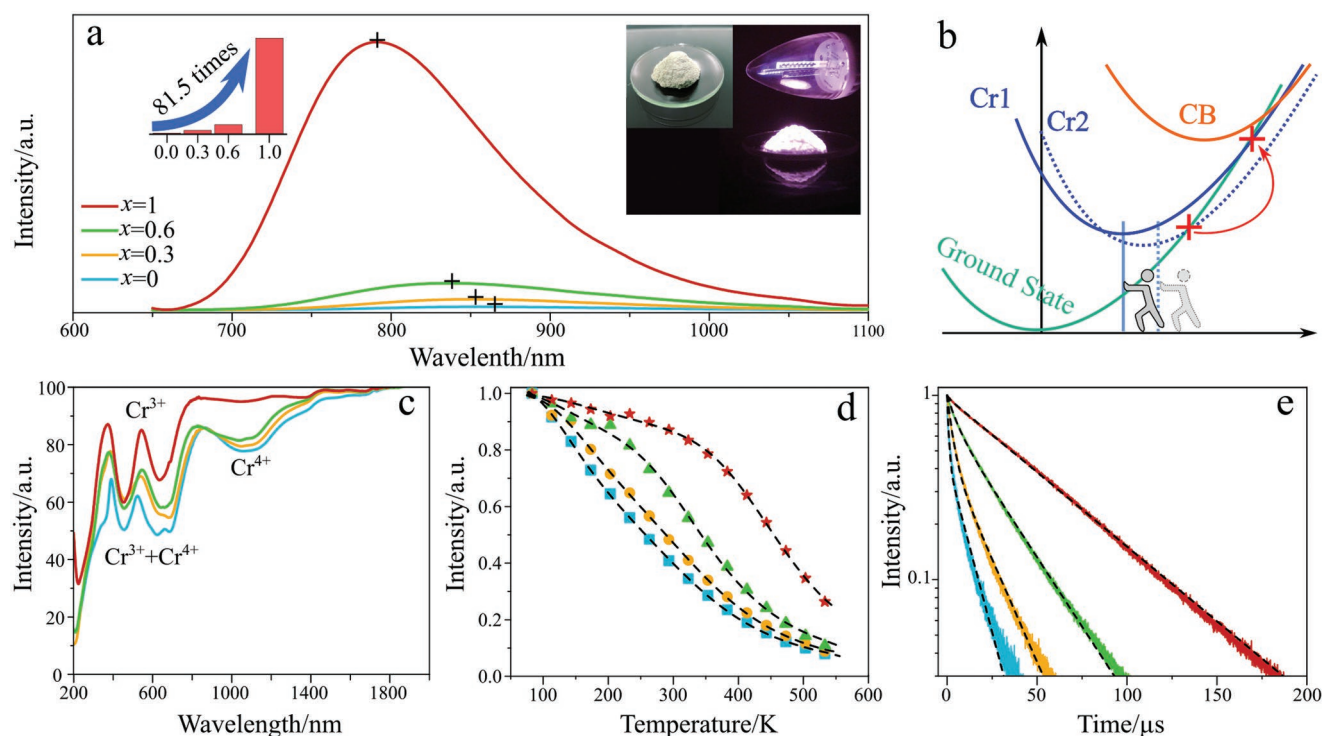


Figure 3. a) Emission spectra, b) configuration coordinate diagram, c) DR spectra, and d) temperature dependence of emission intensities of $\text{Ca}_{3-x}\text{Lu}_x\text{Hf}_2\text{Al}_{2+x}\text{Si}_{1-x}\text{O}_{12}:0.08\text{Cr}^{3+}$ excited by 460 nm. e) Fluorescence decay curves of $\text{Ca}_{3-x}\text{Lu}_x\text{Hf}_2\text{Al}_{2+x}\text{Si}_{1-x}\text{O}_{12}:0.08\text{Cr}^{3+}$ excited by 460 nm and monitored at 750 nm.

are measured. It is observed that the emission band excited by 280 nm locates at shorter wavelength side of that excited by 460 nm. Moreover, the longer wavelength band evolves toward the shorter one with increasing x . Finally, the two bands almost coincide completely with the peak around 785 nm.

The experiment results show two Cr^{3+} centers, one of which is responsible for the 785 nm emission band (Cr1) and is the dominant center for $x = 1$. The Cr1 emission is also observed for $x = 0$ excited by 280 nm but with a broader bandwidth. The band broadening is attributed to the overlap with the emission of the other Cr^{3+} center (Cr2) peaked at a longer wavelength of 855 nm, which dominates the emission spectrum under 460 nm excitation (Figure S6e, Supporting Information). The observed evolution of the 460 nm excited emission band toward the 280 nm excited emission band with increasing x suggests that the number ratio of Cr1 to Cr2 increases, resulting in blue shift of the emission spectra (Figure 3a). The luminescent properties of the phosphors are therefore contributed by the two Cr^{3+} centers and determined by their number ratio depending on x . The two Cr^{3+} centers are similar to that observed in $\text{Ca}_2\text{LuZr}_2\text{Al}_3\text{O}_{12}:\text{Cr}^{3+}$ in our previous work.^[21]

The remarkable emission intensity enhancement is attributed to the increased total number of the two Cr^{3+} centers. Valence conversion from Cr^{4+} to Cr^{3+} with increasing x is observed as shown in Figure 3c. When $x = 0$, the characteristic absorption peak of $\text{Cr}^{4+} 4\text{T}_1 \rightarrow 4\text{T}_2$ transition in the range of 800–1400 nm is strong. With increasing x , the absorption decreases and finally disappears when $x = 1$. Reduction of Cr^{4+} to Cr^{3+} is caused by charge compensation when $[\text{Lu}^{3+}-\text{Al}^{3+}]$ substituting for $[\text{Ca}^{2+}-\text{Si}^{4+}]$. When $x = 0$, one third of the

tetrahedral sites are occupied by Si^{4+} , which offers tetravalent sites for Cr^{4+} . With $[\text{Lu}^{3+}-\text{Al}^{3+}]$ substituting for $[\text{Ca}^{2+}-\text{Si}^{4+}]$, the tetravalent tetrahedral site disappears when $x = 1$. Evidence of this process is the luminescence of Cr^{4+} shown in Figure S9b (Supporting Information). According to previous reports, Cr^{4+} only shows luminescence in tetrahedral site of garnet.

Cr1 is more efficient compared with Cr2 for smaller electron–phonon coupling, which can be explained by the configuration coordinate diagram in Figure 3b. Thermal quenching occurs by nonradiative transition through the intersection of excited state and ground state. The potential energy curve of Cr1 excited state locates at the left side of Cr2 for smaller Stokes shift. The intersection of Cr1 excited state is, therefore, higher than that of Cr2 and a slower nonradiative process in Cr1 is expected. Accordingly, the reduction of the emission intensity of $\text{Ca}_{3-x}\text{Lu}_x\text{Hf}_2\text{Al}_{2+x}\text{Si}_{1-x}\text{O}_{12}:0.08\text{Cr}^{3+}$ depending on temperature becomes slower with increasing x value, as shown in Figure 3d. The room temperature emission intensity for $x = 1$ keeps 87.1% of its low temperature intensity, while that for $x = 0$ keeps only 40.8%. Two thermal processes are recognized by their different thermal activation energies (ΔE), as shown in Figure S11 (Supporting Information) and listed in Table S6 (Supporting Information). ΔE of Cr1 at both high and low temperature processes are much larger than that of Cr2. The 0–260 °C high-temperature range shows ΔE of 0.353 eV, which is similar to 0.36 eV of $\text{ScBO}_3:\text{Cr}^{3+}$ (0–250 °C).^[22] Another evidence for the slow nonradiative process of Cr1 is the observation of slower fluorescence decay for $x = 0$ compared with that for $x = 1$, as shown in Figure 3e. The fluorescence lifetime is only 6.05 μs when Cr2 is

the dominant luminescence center ($x = 0$) and increases to $51.94 \mu\text{m}$ when Cr1 is dominant ($x = 1$).

2.3. NIR pc-LED Device

A broadband NIR pc-LED is fabricated by coating $\text{Ca}_2\text{LuHf}_2\text{Al}_3\text{O}_{12}:0.08\text{Cr}^{3+}$ ($x = 1$) phosphor on a commercial 460 nm LED chip, as shown in Figure 4a,b. When the NIR pc-LED is lit up, the images of the NIR pc-LED are taken by a visible camera and an NIR camera, respectively, as shown in Figure 4c. Photoelectric property of the NIR pc-LED is measured and depicted in Figure 4d. The NIR output power of the pc-LED reaches 46.09 mW under forward current of 100 mA. This is a great improvement compared to the previously reported value of $\approx 26 \text{ mW}@100 \text{ mA}$.^[22,23] A further improved output power of 54.29 mW is achieved under 130 mA current. The photoelectric efficiency of the NIR pc-LED is 21.28%@10 mA and decreases to 15.75%@100 mA. The photoelectric efficiency decreases with increasing current and is caused by efficiency droop effect^[34] of the blue LED chip. Figure 4e shows the electroluminescence spectra of the NIR pc-LED under different currents.

Spectra of the NIR light from the NIR pc-LED after passing through the finger, palm, wrist, and upper arm, respectively, are shown in Figure 5a. The experimental setup is shown in Figure 5b. The spectra only show the broadband NIR emission of the phosphor. The blue emission of the LED chip is blocked by the tissues. The NIR light is detected with peak intensity of $32.1 \mu\text{W nm}^{-1}$ after passing through the finger. That value reduces to $1.2 \times 10^{-2} \mu\text{W nm}^{-1}$ after passing through the upper arm ($\approx 8 \text{ cm}$). The strong light attenuation is caused by scattering of tissues since the scattering coefficients ($0.5\text{--}10 \text{ mm}^{-1}$) of most tissues are much larger than the absorption coefficients ($0.005\text{--}0.02 \text{ mm}^{-1}$).^[35,36] The large penetrate depth is ascribed to the high power of the NIR pc-LED ($46.09 \text{ mW}@100 \text{ mA}$). The

photos of the NIR light passing through the palm and finger are illustrated in Figure 5d. Blood vessels in the finger and palm can be clearly observed by chiaroscuro due to absorption of NIR light by chromophores in blood. To show the lighting effect, the NIR pc-LED is lit up in the dark to brighten the logo printed on an A4 paper sheet, as shown in Figure 5c.

2.4. Application

Transmission spectra of some substances such as water, alcohol, and bovine hemoglobin are measured by using the NIR pc-LED as light source. The experimental setup is shown in Figure 6a. For comparison, the transmission spectra of water and alcohol are measured by the NIR pc-LED and UV-vis-NIR spectrometer (UV-3600plus, Shimadzu), respectively. As shown in Figure 6c,d, the main absorption bands at 900 nm of alcohol and 975 nm of water are recognized by the NIR pc-LED. Even the weak absorption band at $\approx 750 \text{ nm}$, $\approx 810 \text{ nm}$ of alcohol and $\approx 740 \text{ nm}$, $\approx 820 \text{ nm}$ of water can also be observed. Furthermore, the transmission spectra of the finger, palm, and wrist were calculated and are shown in Figure 6g. Two broad absorption bands at 700–800 nm and 800–1050 nm are observed. The absorption at 700–800 nm is ascribed to deoxyhemoglobin (deoxy-Hb). Absorption at 800–1050 nm can be divided into three sub-bands ≈ 835 , ≈ 890 , and $\approx 970 \text{ nm}$, which is ascribed to cytochrome c oxidase (CCO, 820–840 nm),^[37] oxyhemoglobin (oxy-Hb), and water, respectively. Oxy-Hb and deoxy-Hb are both hemoglobin named according to oxygen binding or not. The structure and characteristic absorption of oxy-Hb and deoxy-Hb are shown in Figure 6e.

Concentration of deoxy-Hb and oxy-Hb can be measured by light attenuation at ≈ 760 and $\approx 890 \text{ nm}$. According to the Beer–Lambert law, the absorbance should show a linear relationship with the concentration. Bovine hemoglobin solutions

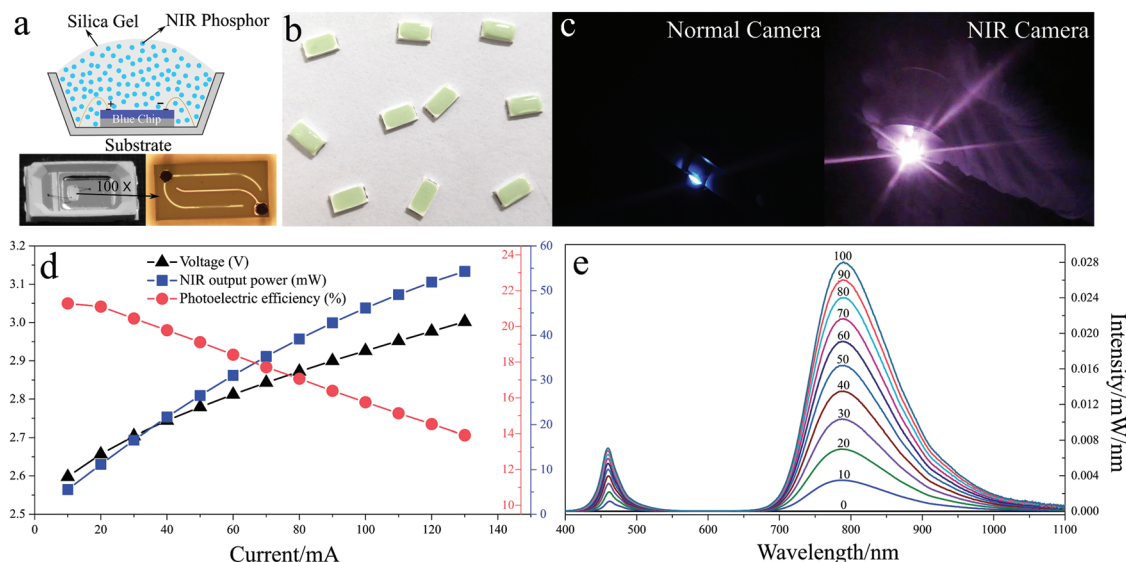


Figure 4. a) Structure diagram and b) photo of the NIR pc-LED fabricated by $\text{Ca}_2\text{LuHf}_2\text{Al}_3\text{O}_{12}:0.08\text{Cr}^{3+}$ ($x = 1$). c) Photos of the NIR pc-LED under 100 mA current taken by a visible and an NIR camera, respectively. d) Dependence of voltage, NIR output power, and photoelectric efficiency on current. e) Electroluminescence spectra of the NIR pc-LED under different currents.

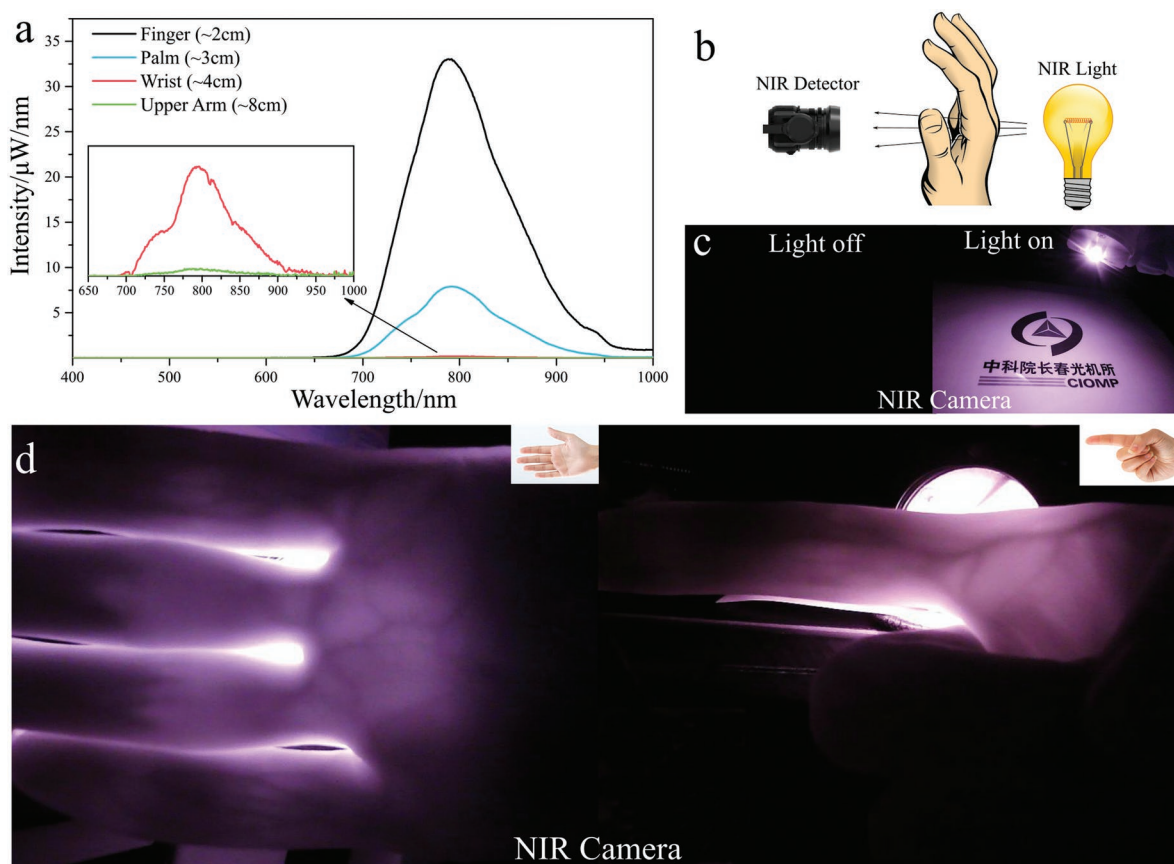


Figure 5. a) Schematic diagram of experimental setup. b) Photo of the NIR pc-LED lights up in dark environment. c) Spectra of light after penetrating different body parts. d) Photos of the NIR light transilluminating palm and finger, respectively. The NIR pc-LED works at 100 mA current.

with different concentration are prepared as calibration. The transmission spectra of the bovine hemoglobin solutions are measured by using the NIR pc-LED, as shown in Figure 7a,b. Different absorption intensity counting methods are adopted to show the linear dependency, as shown in Figure 7c–h. The integral intensity at 600–1000 nm shows the best linear correlation with Pearson correlation coefficient of 0.9992.

3. Conclusion

The emission intensity enhancement by a factor of 81.5 is achieved in $\text{Ca}_{3-x}\text{Lu}_x\text{Hf}_2\text{Al}_{2+x}\text{Si}_{1-x}\text{O}_{12}:\text{Cr}^{3+}$ garnet phosphor with x increasing from 0 to 1. Spectrum analysis shows two Cr^{3+} centers with emission band peaked at 785 nm (Cr1) and 855 nm (Cr2), respectively. With increasing x , Cr^{4+} is reduced to Cr^{3+} and the number ratio of Cr1 to Cr2 increases due to chemical unit co-substitution of $[\text{Lu}^{3+}-\text{Al}^{3+}]$ for $[\text{Ca}^{2+}-\text{Si}^{4+}]$. As a result, the greatly enhanced emission intensity with blue shift is observed. Crystal structure and electronic structure analysis were performed by Rietveld refinement and first-principles calculations, respectively. Changes in local disorder of the dodecahedral and tetrahedral sites are proved by Raman spectra. CBM also changes from the hybrid electronic states of Hf^{4+} and Ca^{2+} to electronic states of Lu^{3+} . NIR pc-LED is fabricated by combining the optimized NIR phosphor $\text{Ca}_2\text{LuHf}_2\text{Al}_3\text{O}_{12}:0.08\text{Cr}^{3+}$

with commercial 460 nm LED chip. The NIR output power is 46.09 mW under 100 mA forward current, which is a great improvement compared with previous results. The improved output power results in large penetrate depth of the NIR light in tissues. For example, the signal of the NIR light can still be detected after passing through the upper arm (≈ 8 cm). Based on NIR spectroscopy, absorption of hemoglobin (oxy-Hb and deoxy-Hb) for blood oxygen detection and CCO for photobiomodulation therapy in the body are observed by the NIR pc-LED. Thus the NIR pc-LED shows great potential in bio-sensing applications.

4. Experimental Section

Synthesis of the Garnet Phosphor: The broadband NIR phosphors were fabricated by a simple solid state method with low cost and good repeatability. Raw materials CaCO_3 (99.99%), Lu_2O_3 (99.9%), HfO_2 (98%), Al_2O_3 (99.9%), SiO_2 (99.9%), and Cr_2O_3 (99.99%) were weighted according to the stoichiometric ratio and grinded in an agate mortar for 60 min. Then, the mixtures were transferred into a tube furnace and sintered at 1600 °C for 4 h. The samples were protected by 5% H_2/N_2 gas during the whole sintering process.

Fabrication of the pc-LED: A 460 nm LED chip was fixed in an SMD 5730 PCB substrate. The electrodes of the LED chip were attached to the substrate by gold thread. Then, the slurry composed of NIR phosphor and silica gel was prepared and coated on the LED chip. The curing process was performed at 120 °C for 20 min in an oven.

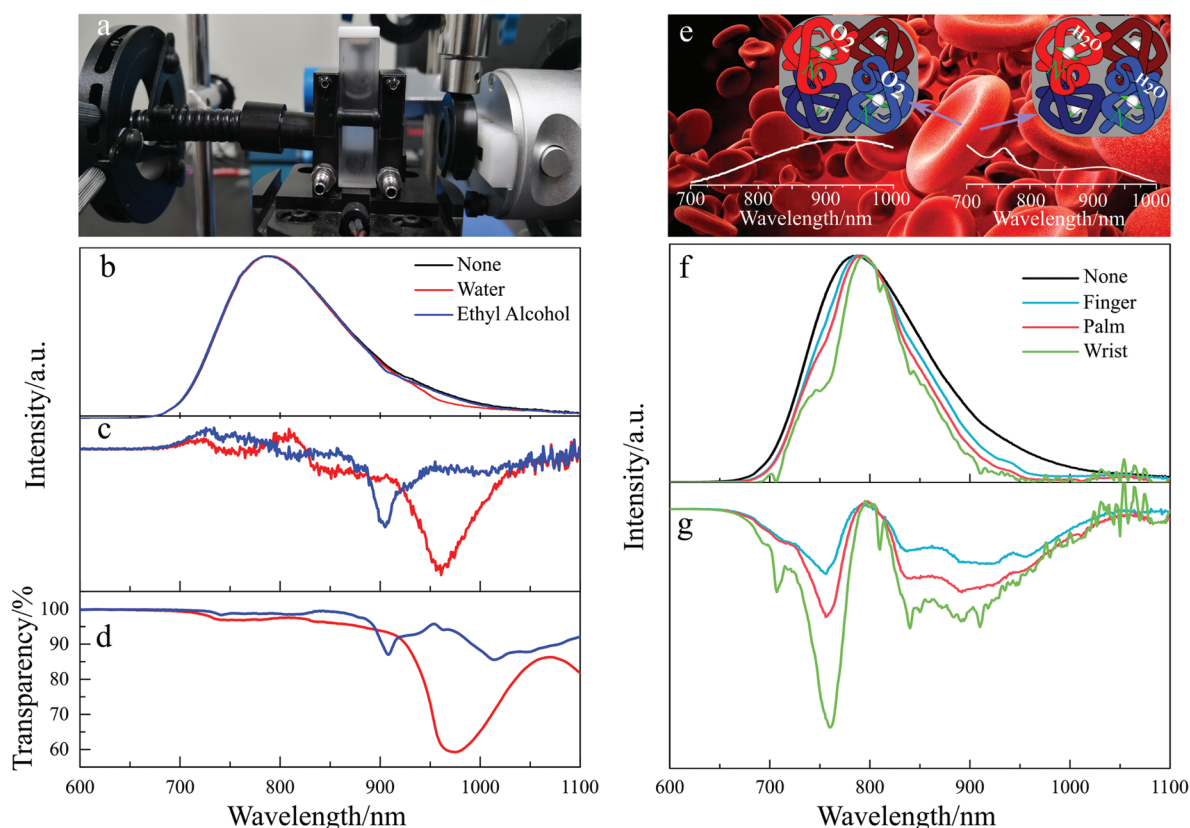


Figure 6. a) Photo of the experimental setup. b) Normalized spectra of NIR light after penetrating water and alcohol, respectively. c) Calculated and d) measured transmission spectra by the NIR pc-LED and spectrometer (3600plus, Shimadzu), respectively. e) Structure and absorption spectra of oxy-Hb and deoxy-Hb. f) Normalized spectra of NIR light after penetrating different body parts. g) Calculated transmission spectra of different body parts by the NIR pc-LED.

Characterization: The first-principles calculations were based on density functional theory using the projected augmented wave method implemented in the Vienna ab-initio simulation package (VASP). To compute the electron exchange–correlation energy, the Perdew–Burke–Ernzerhof generalized gradient approximation was used. The cutoff energy for the plane wave basis set was 408 eV. The optimized geometries were obtained with all the atomic positions relaxed until

their residual forces were less than $0.01 \text{ eV } \text{\AA}^{-1}$. A Monkhorst–Pack K -mesh for the Brillouin-zone integration with K -point separation of 0.03 and 0.02 \AA^{-1} was applied for the structure optimization and DOS, respectively. Rietveld refinement of X-ray diffraction (XRD) pattern was performed by FullProf program using data collected in Bruker D8 Focus diffractometer (Cu $K\alpha$, 40 kV, 40 mA) with count time of 5 s per step and step size of 0.02° . The excitation spectra

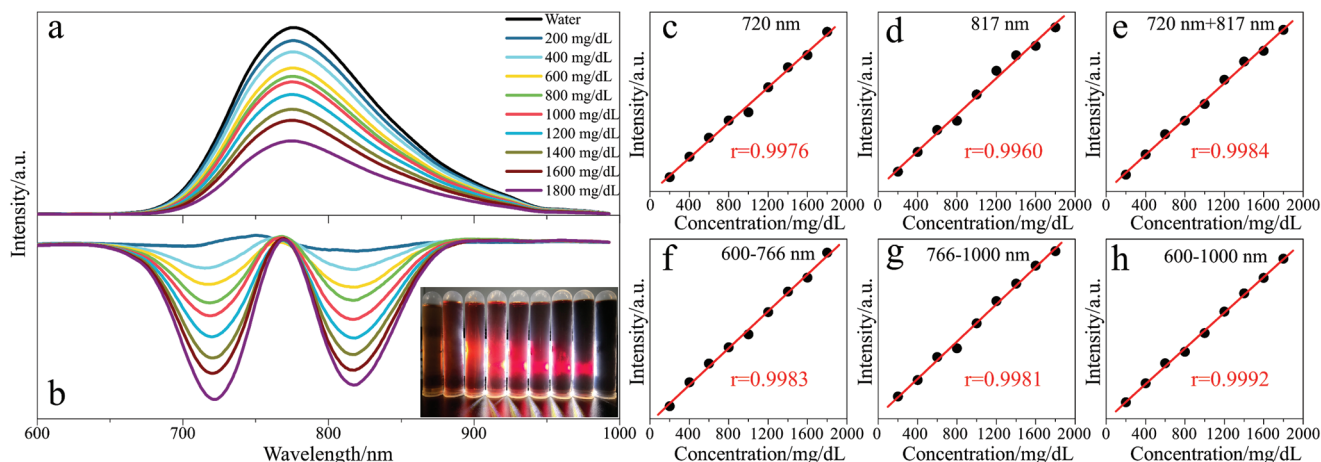


Figure 7. a) Spectra of NIR light after penetrating bovine hemoglobin solution with different concentration. b) Calculated transmission spectra. c–h) Relationships between absorption intensity by different counting methods and concentration of bovine hemoglobin solution. The counting methods include c) peak intensity at 720 nm of deoxy-Hb, d) peak intensity at 817 nm of oxy-Hb, e) sum of intensities at 720 and 817 nm, f) integral intensity at 600–766 nm, g) integral intensity at 766–1000 nm, and h) integral intensity at 600–1000 nm.

and DR spectra were measured by FL910 spectrometer (Edinburgh Instruments) and UV-vis-NIR spectrometer (UV-3600plus, Shimadzu, Japan), respectively. The elementary composition measurement was made in an Energy-dispersive X-ray spectroscopy equipped in a field emission scanning electron microscopy (S-4800, Hitachi, Japan). The temperature dependence properties were measured on the Olympus BX53M fluorescence microscopy system. The system is composed of a 130 W short arc mercury lamp (U-HGLGPS, 130W, Olympus), 77–873 K cooling–heating platform (THMS600E, Linkam Scientific Instruments), and 200–1000 nm microfiber spectrometer (QEPro, Ocean Optics). The emission spectra and photoelectric properties of the pc-LEDs were measured by a photoelectric measuring system (HAAS 2000, 350–1100 nm, EVERFINE). The system is composed of DC electrical source (0–5A, 0–30 V, ± 0.2), integrating sphere (SPEKTRON R98, $\phi 80$ cm), and spectrometer (HAMAMATSU, TE-cooled CCD).

Supporting Information

Supporting Information is available from the Wiley Online Library or from the author.

Acknowledgements

This work was partially supported by the National Natural Science Foundation of China (Grant Nos. 11604330, 11874055, and 51772286), the National Key R&D Program of China (Grant Nos. 2016YFB0400605, 2016YFB0701003, and 2017YFB0403104), and the Natural Science Foundation of Jilin Province (Grant No. 20160520171JH).

Conflict of Interest

The authors declare no conflict of interest.

Keywords

broadband emission, chromium doping, light-emitting diodes, near-infrared spectroscopy, phosphors

Received: January 29, 2019
Revised: March 27, 2019
Published online:

- [1] A. T. Eggebrecht, S. L. Ferradal, A. R. Viehoveer, M. S. Hassanpour, H. Dehghani, A. Z. Snyder, T. Hershey, J. P. Culver, *Nat. Photonics* **2014**, *8*, 448.
- [2] B. Zeng, Z. Huang, A. Singh, Y. Yao, A. K. Azad, A. D. Mohite, A. J. Taylor, D. R. Smith, H. Chen, *Light: Sci. Appl.* **2018**, *7*, 51.
- [3] M. Watari, *Opt. Rev.* **2010**, *17*, 317.
- [4] C. Pasquini, *Anal. Chim. Acta* **2018**, *1026*, 8.
- [5] A. Muhammad, X. Zou, E. T. Haroon, X. Hu, R. Allah, B. Sajid, H. Zhao, *J. Food Meas. Charact.* **2018**, *12*, 2366.
- [6] A. E. Draghici, D. Potart, J. L. Hollmann, V. Pera, Q. Fang, C. A. Dimarzio, J. A. Taylor, M. J. Niedre, S. J. Shefelbine, *J. Orthop. Res.* **2018**, *36*, 183.
- [7] M. Lukovic, V. Lukovic, I. Belca, B. Kasalica, I. Stanimirovic, M. Vivic, *J. Eur. Opt. Soc.-Rapid* **2016**, *12*, 19.
- [8] T. Pulli, T. Donsberg, T. Pikeonen, F. Manoocheri, P. Karha, E. Ikonen, *Light Sci. Appl.* **2015**, *4*, e332.
- [9] H. Chen, R. Zhu, J. He, W. Duan, W. Hu, Y. Lu, M. Li, S. Lee, Y. Dong, S. Wu, *Light Sci. Appl.* **2016**, *6*, e17043.
- [10] S. Abe, J. J. Joos, L. I. Martin, Z. Hens, P. F. Sme, *Light Sci. Appl.* **2017**, *6*, e16271.
- [11] K. Oshima, K. Terasawa, S. Fuchi, Y. Takeda, *Phys. Status Solidi c* **2012**, *9*, 2340.
- [12] S. Fuchi, A. Sakano, R. Mizutani, Y. Takeda, *Appl. Phys. Express* **2009**, *2*, 032102.
- [13] S. Nishimura, S. Fuchi, Y. Takeda, *J. Mater. Sci.: Mater. Electron.* **2017**, *28*, 7157.
- [14] S. Fuchi, A. Sakano, R. Mizutani, Y. Takeda, *Appl. Phys. B* **2011**, *105*, 877.
- [15] S. Fuchi, Y. Takeda, *Phys. Status Solidi c* **2011**, *8*, 2653.
- [16] S. Fuchi, A. Sakano, Y. Takeda, *Jpn. J. Appl. Phys.* **2008**, *47*, 7932.
- [17] H. Uemura, S. Fuchi, R. Kato, K. Amano, K. Hiraizumi, H. Hayase, Y. Takeda, *J. Phys.: Conf. Ser.* **2015**, *619*, 012053.
- [18] S. Moller, A. Katalnikovas, M. Hasse, T. Justel, *J. Lumin.* **2016**, *172*, 185.
- [19] R. A. Talewar, S. Mahamuda, A. Joshi, S. V. Moharil, *J. Lumin.* **2018**, *202*, 1.
- [20] D. Yu, R. Martin-Rodriguez, Q. Zhang, A. Meijerink, F. T. Rabouw, *Light Sci. Appl.* **2015**, *4*, e344.
- [21] L. Zhang, S. Zhang, Z. Hao, X. Zhang, G. Pan, Y. Luo, H. Wu, J. Zhang, *J. Mater. Chem. C* **2018**, *6*, 4967.
- [22] Q. Shao, H. Ding, L. Yao, J. Xu, C. Liang, J. Jiang, *RSC Adv.* **2018**, *8*, 12035.
- [23] Q. Shao, H. Ding, L. Yao, J. Xu, C. Liang, Z. Li, Y. Dong, J. Jiang, *Opt. Lett.* **2018**, *43*, 5251.
- [24] V. Rajendran, M. Fang, G. Guzman, T. Lesniewski, S. Mahlik, M. Grinberg, G. Leniec, S. Kaczmarek, Y. Lin, K. Lu, C. Lin, H. Chang, S. Hu, R. Liu, *ACS Energy Lett.* **2018**, *3*, 2679.
- [25] W. Huang, C. Cheng, Z. Bao, C. Yang, K. Lu, C. Kang, C. Lin, R. Liu, *Angew. Chem., Int. Ed.* **2019**, *58*, 1.
- [26] X. Li, J. D. Budai, F. Liu, J. Y. Howe, J. Zhang, X. Wang, Z. Gu, C. Sun, *Light Sci. Appl.* **2013**, *2*, e50.
- [27] T. Senden, R. Dijk-Moes, A. Meijerink, *Light Sci. Appl.* **2018**, *7*, 8.
- [28] M. Casalboni, A. Luci, U. M. Grassano, *Phys. Rev. B* **1994**, *49*, 3781.
- [29] M. Grinberg, *Phys. Rev. B* **1995**, *52*, 3917.
- [30] M. Back, J. Ueda, M. G. Brik, T. Lesniewski, M. Grinberg, S. Tanabe, *ACS Appl. Mater. Interfaces* **2018**, *10*, 41512.
- [31] M. Allix, S. Chenu, E. Veron, T. Pourmeyrol, E. A. Kouadri-Boudijelthia, S. Alahrache, F. Porcher, D. Massiot, F. Fayon, *Chem. Mater.* **2013**, *25*, 1600.
- [32] Z. Xia, Q. Liu, *Prog. Mater. Sci.* **2016**, *84*, 59.
- [33] Z. Xia, C. Ma, M. S. Molokeev, Q. Liu, K. Rickert, K. R. Poeppelmeier, *J. Am. Chem. Soc.* **2015**, *137*, 12494.
- [34] V. A. Jhalani, J. J. Zhou, M. Bernardi, *Nano Lett.* **2017**, *17*, 5012.
- [35] H. T. Whelan, R. L. Smits, E. V. Buchmann, *J. Clin. Laser Med. Surg.* **2001**, *19*, 305.
- [36] D. T. Delpy, M. Cope, *Phil. Trans. R. Soc. Lond. B: Biol. Sci.* **1997**, *352*, 649.
- [37] F. F. Jobsis, *Science* **1977**, *198*, 1264.